Cement and Concrete Research 41 (2011) 311–323

Contents lists available at ScienceDirect

Cement and Concrete Research

journal homepage: http://ees.elsevier.com/CEMCON/default.asp

Iron in carbonate containing AFm phases

B.Z. Dilnesa [a,*], B. Lothenbach [a], G. Le Saout [a], G. Renaudin [b,c], A. Mesbah [b,c], Y. Filinchuk [d,1], A. Wichser [a], E. Wieland [e]

[a] Empa, Laboratory for Concrete & Construction Chemistry, Überlandstrasse 129, CH-8600 Dübendorf, Switzerland
[b] Clermont Université, ENSCCF, Laboratoire des Matériaux Inorganiques, BP 10448, F-63000 Clermont-Ferrand, France
[c] CNRS, UMR 6002, LMI, F-63177 Aubière, France
[d] Swiss-Norwegian Beam Lines at ESRF, 6 rue Jules Horowitz, BP 220, 38043 Grenoble, France
[e] Paul Scherrer Institute, Nuclear Energy and Safety Research Department, Laboratory for Waste Management, 5232 Villigen PSI, Switzerland

ARTICLE INFO

Article history:
Received 6 September 2010
Accepted 23 November 2010

Keywords:
Crystal structure (B)
AFm phases (D)
Solubility product (B)
Solid solution (B)
Monocarbonate (D)

ABSTRACT

One of the AFm phases in hydrated Portland cement is $Ca_3(Al_xFe_{2-x})O_6.CaCO_3.nH_2O$. It is based on hexagonal and platey structural elements and the interlayer structure incorporates CO_3^{2-}. The solid phases were experimentally synthesized and characterized by different techniques including X-ray techniques (XRD and EXAFS) and vibrational spectroscopy techniques (IR, Raman). Fe-monocarbonate (Fe-Mc) and Al-monocarbonate (Al-Mc) were found to be stable up to 50 °C, while Fe-hemicarbonate (Fe-Hc) was unstable with respect to Fe-Mc in the presence of calcite. Fe-Mc has a rhombohedral $R\bar{3}c$ symmetry which is different from the triclinic of the Al analogue. Both XRD and thermodynamic modelling of the liquid compositions indicated that Al-Mc and the Fe-Mc phases do not form solid solution. The solubility products were calculated experimentally at 20 °C and 50 °C. Under standards condition the solubility products and other thermodynamic parameters were estimated using temperature-solubility product extrapolation and found to be $\log K_{S0}$ (Fe-Mc) $= -34.59 \pm 0.50$, $\log K_{S0}$ (Fe-Hc) $= -30.83 \pm 0.50$ and $\log K_{S0}$(Al-Mc) $= -31.32 \pm 0.50$.

1. Introduction

The main hydration products of Portland cements include C–S–H (calcium silicate hydrate), portlandite, ettringite and AFm (Al_2O_3–Fe_2O_3-mono) phases. AFm phases are formed from C_3A ($3CaO\cdot Al_2O_3$) and C_4AF ($4CaO\cdot Al_2O_3\cdot Fe_2O_3$) phases in the presence of carbonates, sulphates, chlorides and hydroxide during the hydration of Portland cement. The general formula is $Ca_2(Al,Fe)(OH)_6X\cdot nH_2O$, where X denotes a single charged or half of a double charged anion which occupies the interlayer sites. Among possible anions are OH^-, SO_4^{2-}, CO_3^{2-} and Cl^-. AFm phases have a layered structure composed of two layers, a positively charged main layer $[Ca_2(Al,Fe)(OH)_6]^+$ and a negatively charged $[X\cdot nH_2O]^-$ interlayer. The main layer consists of sheets of $Ca(OH)_6$ octahedral ions, as in portlandite, in which every third Ca^{2+} is substituted by Al^{3+} and/or Fe^{3+}.

Cements are sensitive to carbonation which can lead to the formation of hemicarbonate $3CaO\cdot(Al_xFe_{1-x})_2O_3\cdot(CaCO_3)_{0.5}\cdot(Ca(OH)_2)_{0.5}\cdot nH_2O$ and/or monocarbonate $3CaO\cdot(Al_xFe_{1-x})_2O_3\cdot(CaCO_3)\cdot mH_2O$, $x = 0$ to 1. Al-monocarbonate (Al-Mc) has a triclinic pseudohexagonal symmetry [1]. The solubility products of Al-monocarbonate and hemicarbonate have been determined experimentally in the range of 5 to 85 °C [2]. The stability of these phases has an impact on the bulk chemistry of cements as the formation of hemi- and/or monocarbonate indirectly stabilizes ettringite. This results in a higher volume of hydrated phases which can contribute to the improvement in mechanical properties of cement pastes [3,4]. It has been shown that Al-hemicarbonate (Al-Hc) and hydroxy-AFm are unstable with respect to Al-monocarbonate in the presence of calcite [3,5].

OPC contains around 3–4% Fe_2O_3. During hydration, Fe-containing AFm and/or Fe-AFt phases may form. The extent to which Fe is present in AFm and AFt-phases will strongly influence the amount of AFt and AFm phases present and thus the volume of the hydrates and the properties of the hydrated cement. Understanding the characteristic of the hydrates in complex cement matrices is important since the material properties of cement-based materials are related to the chemical environment and the thermodynamic properties of the hydrated phases.

Until recently only rough estimates of the solubility products of Fe-containing monocarbonate and hemicarbonate have been available [6], where the solubility was estimated based on the solubility of the Al-containing phases. The first experimental data on the solubility of Fe-monocarbonate were estimated from Fe-ettringite experiments where contamination with CO_2 led to the formation of Fe-Mc [7].

The formation of solid solutions can play an important role in stabilizing these solids. Solid solutions between anions in the

---

[*] Corresponding author. Empa, Swiss Federal Laboratories for Materials Science and Technology, Laboratory for Concrete and Construction Chemistry, Überlandstrasse 129, 8600 Dübendorf, Switzerland. Tel.: +41 44 823 4947; fax: +41 44 823 4035.
E-mail address: belay.dilnesa@empa.ch (B.Z. Dilnesa).

[1] Present address: Institute of Condensed Matter and Nanosciences, Université Catholique de Louvain, Place L. Pasteur, B-1348, Louvain-la-Neuve, Belgium.

0008-8846/$ – see front matter © 2010 Elsevier Ltd. All rights reserved.
doi:10.1016/j.cemconres.2010.11.017

interlayer structure of Al-containing AFm phases are common [8–10]. The existence of a solid solution between the Al- and Fe-ettringite has been reported [11]. It is unclear, however, to which extent Fe and Al in the main layer of AFm phases form solid solutions.

In this study Fe-containing monocarbonate and hemicarbonate and the solid solution series with their aluminium analogues were synthesized to study their structure and solubility. Different techniques were used to characterize the synthesized solids. Synchrotron X-ray powder diffraction and Raman spectroscopy were used to determine the crystal structure of the Fe-monocarbonate. The solubility products of Fe-Mc and Fe-Hc were determined experimentally and compared with their Al analogues. The solubility products were used together with thermodynamic data for the other cement minerals [6] to model the hydrate assemblages of hydrated Portland cement in the presence of $CaCO_3$ and $CaSO_4$.

2. Materials and methods

2.1. Synthesis of solids

C_3A ($3CaO{\cdot}Al_2O_3$) and C_2F ($2CaO{\cdot}Fe_2O_3$) clinkers were used as starting materials for the synthesis. C_3A and C_2F were prepared by mixing appropriate amounts of $CaCO_3$ with Al_2O_3 and Fe_2O_3 powders and burning at 1400 °C and 1350 °C, respectively for 24 h. CaO was synthesized by burning $CaCO_3$ at 1000 °C.

Pure Fe-Mc and Fe-Hc were synthesized by the addition of appropriate amounts of C_2F, $CaCO_3$, and CaO to 0.1 M KOH solution (50 ml) at liquid/solid ratio ~20 according to:

$$2CaO{\cdot}Fe_2O_3 + CaCO_3 + CaO + 12H_2O \rightarrow 3CaO{\cdot}Fe_2O_3{\cdot}CaCO_3{\cdot}12H_2O$$

$$2CaO{\cdot}Fe_2O_3 + 0.5CaCO_3 + 1.5CaO + 10H_2O \rightarrow 3.5CaO{\cdot}Fe_2O_3{\cdot}(CaCO_3)_{0.5}{\cdot}10H_2O$$

0.1 M KOH solution was used to mimic the high pH present in the pore solution of Portland cement. Al/Fe-monocarbonates were synthesized by precipitation from supersaturated solutions. Appropriate amounts of C_3A, C_2F, $CaCO_3$, and CaO were added to 0.1 M KOH solution (pH = 13.0). The mole fraction of Al varied from x = 0 to 1. The overall stoichiometric reaction is given by:

$$xC_3A + (1-x)C_2F + CaCO_3 + (1-x)CaO + nH_2O \rightarrow 3CaO{\cdot}(Al_xFe_{1-x})_2O_3{\cdot}CaCO_3{\cdot}nH_2O.$$

The samples were stored in closed PE-bottles at different temperatures (20, 50 and 80 °C) and sampled after different reaction times. After equilibration the solid and liquid phases were separated by vacuum filtration through 0.45 μm nylon filters. All sample preparation and handling were done in a glove box filled with N_2-atmosphere to minimize CO_2 contamination.

The mixes used in the undersaturation experiments corresponded to those prepared for the oversaturation experiments. After an equilibration time of 3 years, an additional amount of 0.1 M KOH solution was added to duplicate the volume of the solution (resulting in undersaturation) and equilibrated for 15 months.

2.2. Characterization of the solid and liquid phases

The residues from filtration were dried in N_2-filled desiccators. The relative humidity of the desiccators was kept at approximately 30% using saturated $CaCl_2$ solutions. After drying for two weeks the solids were ground manually to a particle size <60 μm.

Environmental scanning electron microscopy (ESEM) Phillips FEG-XL30 and Infrared spectroscopy (FTS 6000 Spectrometer using KBr pellets technique) were used to characterize the solid phases. The IR spectra were collected in transmission mode in the region 4000 cm^{-1} to 600 cm^{-1}.

Thermogravimetric analysis (TGA) was carried out to determine the water loss and to estimate the concentration of the carbonate anions in the solid phases. The analysis was carried out in N_2 on about 8–12 mg of crushed material at 20 °C/min heat rate over the temperature range from 30–980 °C using a Metter Toledo TGA instrument.

X-ray powder diffraction was carried out using CuKα radiation on a PANalytical X'Pert Pro MPD diffractometer in a θ–2θ configuration with an angular scan 5°–65° 2θ and an X'Celerator detector. To study the effect of relative humidity, a climatic chamber (Anton Paar) specially designed for the X-ray diffractometer in a θ-θ configuration was used. The sample was placed in a sample tray of the climatic chamber of the X-ray diffractometer where both temperature and relative humidity can be controlled. Synchrotron powder diffraction data were collected at Swiss-Norwegian Beam Line (SNBL) at the European Synchrotron Radiation Facility (ESRF), Grenoble, France. The powder material was introduced into glass capillaries (0.5 mm diameter). Data collection was performed at 295 K at a wavelength of $\lambda = 0.72085$ Å using a MAR345 image plate detector with the highest resolution (3450 × 3450 pixels with a pixel size of 100 μm). The calculated absorption coefficient $m\mu R$ (m = powder packing factor, μ = linear absorption coefficient, R = radius of the capillary) was estimated at 0.65. Three sample-to-detector distances were used (150, 250 and 350 mm) in order to combine the advantages of high resolution and extended 2θ range. The detector parameters and the wavelength were calibrated with NIST LaB_6. The exposure time was 60 s with a rotation of the capillary by 60°. The two-dimensional data were integrated with the Fit2D program which produced the correct intensity in relative scale [12]. This 2D detector was used in order to perfectly define the background, to observe very weak diffraction peaks, and to improve the accuracy of the integrated intensities by achieving a better powder average. Uncertainties of the integrated intensities were calculated at each 2θ-point applying Poisson statistics to the intensity data, considering the geometry of the detector. The Instrument Resolution Function was determined from the LaB_6 data.

Micro-Raman spectra were recorded at room temperature in the back scattering geometry, using a Jobin-Yvon T64000 device. The Raman detector was a charge coupled device (CCD) multichannel detector cooled by liquid nitrogen to 140 K. The laser beam was focused onto the sample through an Olympus confocal microscope with x100 magnification. The laser spot was about 1 μm². The spectral resolution obtained with an excitation source at 514.5 nm (argon ion laser line, spectra physics 2017) was about 1 cm^{-1}. The measured power at the sample level was kept low (<5 mW) in order to avoid any damage of the material. The Raman scattered light was collected with microscope objectives at 360° angle from the excitation and filtered with an holographic Notch filter before being dispersed by a single grating (1800 grooves per mm).

Synchrotron-based extended X-ray absorption fine structure (EXAFS) spectroscopy was used to determine the coordination environment of Fe in Fe-Mc. The spectra were collected at the Fe K-edge (7112 eV) at beamline 26A (Dubble) at ESRF, Grenoble, France. The beamline is equipped with a Si (111) crystal monochromator. The monochromator angle was calibrated by assigning the energy of 7112 eV to the first inflection point of the K-adsorption edge of Fe metal foil. The EXAFS measurements were carried out at room temperature in transmission using ionization chambers (Oxford Instruments).

Reduction and modelling of the EXAFS data was performed with the IFEFFIT (ATHENA/ ARTEMIS) software package following standard procedures [13,14]. After background subtraction, the energy was converted to photoelectron wave vector units ($Å^{-1}$) by assigning the ionization energy of the iron K-edge (7112 eV), E_0, to the first inflection point of the absorption edge. The radial structural function (RSF) was obtained by Fourier transforming k^3-weighted $\chi(k)$ functions between 2.0 and 11.5 $Å^{-1}$ using a Kaiser–Bessel window function with a smoothing parameter of 4. A multi shell approach was employed for data fitting. Theoretical single scattering paths were calculated with FEFF8 using the Al-Mc structure as model compounds. The amplitude reduction factor (S_0^2) was set at 0.75.

A pH electrode (Knick pH-meter 766 with a Knick SE 100 pH/Pt 1000 electrode) was used to measure the OH^- concentrations in an aliquot of the undiluted solutions immediately after filtration. Before the measurements the electrode was calibrated with KOH-solutions of known concentrations. Another aliquot was diluted by a factor of 10 with HNO_3 (6.5% supra-pure) and analyzed for S, Ca, Al and K by inductively-coupled plasma optical emission spectrometry (ICP/OES; Varian, VISTA Pro) and for iron by inductively-coupled plasma mass spectrometry (ICP/MS; Finnigan MAT, ELEMENT2).

2.3. Thermodynamic modeling

Thermodynamic modeling was carried out using the geochemical code GEMS [15]. GEMS is a broad-purpose geochemical modeling code, which computes equilibrium phase assemblage and speciation in a complex chemical system from its total bulk elemental composition. Chemical interactions involving solids, solid solutions, gas mixture and aqueous electrolyte are considered simultaneously. The default database of GEMS code was used, which is based on the PSI chemical thermodynamic database [16] merged with the slop98.dat database for temperature and pressure corrections [17]. The activity coefficients of aqueous species y_i were computed with the built-in expanded extended Debye–Hückel equation in Truesdell–Jones form with individual parameters a_i (dependent on ion size) and common third parameter b_y:

$$log\lambda_i = \frac{-A_y z_i^2 \sqrt{I}}{1 + B_y a_i \sqrt{I}} + b_y I \tag{1}$$

where z_i denotes the charge of species i, I the effective molal ionic strength, b_y is a semi-empirical parameter (0.064 at 25 °C), and A_y and B_y are P,T-dependent coefficients. This activity correction is thought to be applicable up to 1–2 M ionic strength [15].

The temperature dependency of the solubility product of Fe-Hc and Fe-Mc were computed based on the solubility measured at 20 and at 50 °C with the help of GEMS, using the built-in three-term temperature extrapolation function given by Eq. (2) and the relationships shown in Eqs. (3)–(5) [18]. The three-term temperature extrapolation assumes that the heat capacity of the reaction, $\Delta_r C_p^0$, is constant in the considered temperature range.

$$logK_T = A_0 + \frac{A_2}{T} + A_3\ lnT; \tag{2}$$

$$A_0 = \frac{0.4343}{R} \cdot \left[\Delta_r S_{T_0}^0 - \Delta_r Cp_{T_0}^0 (1 + \ lnT_0)\right] \tag{3}$$

$$A_2 = -\frac{0.4343}{R} \cdot \left(\Delta_r H_{T_0}^0 - \Delta_r Cp_{T_0}^0\, T_0\right) \tag{4}$$

$$A_3 = \frac{0.4343}{R} \cdot \Delta_r Cp_{T_0}^0 \tag{5}$$

where T_0 is the reference temperature (298.15 K) and S° the entropy. A more detailed description of the temperature corrections used in GEMS is given elsewhere [19] and in the online documentation of GEMS.

The entropy S° was adjusted to obtain the best fit between the measured solubility data at different temperatures and the calculated solubility products. As only a two solubility measurements at different temperatures have been carried out, only the entropy was fitted, while the heat capacities Cp° for Fe-Mc and Fe-Hc was calculated based on a reference reaction with the structurally similar Al-monosulphate with known Cp° [20] according to:

$$3CaO \cdot Fe_2O_3 \cdot CaCO_3 \cdot 12H_2O \Leftrightarrow 3CaO \cdot Al_2O_3 \cdot CaSO_4 \cdot 12H_2O - Al_2O_3 - CaSO_4 + Fe_2O_3 + CaCO_3$$

$$3CaO \cdot Fe_2O_3 \cdot (CaCO_3)_{0.5} \cdot (CaO)_{0.5} \cdot 10H_2O \Leftrightarrow 3CaO \cdot Fe_2O_3 \cdot CaCO_3 \cdot 12H_2O - 0.5CaCO_3 - 2Ca(OH)_2 + 2.5CaO$$

If such reference reactions involve only solids and no “free” water, the change in heat capacity and the entropy is approximately zero [21]. Tables 1 and 2 summarize the thermodynamic data used in this study.

3. Results and discussion

3.1. Fe-hemicarbonate

The formation of Fe-Hc was studied at different equilibration times in samples containing less calcite than the samples used to prepare Fe-Mc. The XRD pattern shows the formation of an AFm phase, labeled Fe-Hc in Fig. 1 with a peak around 7.48 Å. It is known from Al-containing AFm phases that generally Al-Hc is formed first and converts to Al-Mc with time if calcite is present [3,5]. As the solutions contain only calcium, iron, hydroxide and carbonate, it was tentatively concluded that the observed phase corresponds to Fe-hemicarbonate. After 180 days and longer, the formation of Fe-Mc was observed. In addition, significant quantities of calcite and portlandite were observed at all times. The red color of the solids indicated the presence of X-ray amorphous iron hydroxide.

Ecker et al [22] also observed a peak at 7.49 Å when the sample was dried at 35% relative humidity, which they attributed to the formation of a triclinic Fe-Mc. They also found a peak at around 8.05 Å that was attributed to Fe-Hc. However, the assignments were done by interpolation of the data from the study of the $3CaO \cdot Al_2O_3 \cdot CaCO_3 \cdot 11H_2O - 3CaO \cdot Fe_2O_3 \cdot CaCO_3 \cdot 12H_2O$ systems and they could not synthesize the phase without the presence of Al.

In the system studied here, free of Al, the peak at 7.48 Å shows no change with variation from 90 to 20% relative humidity in the XRD in situ climate chamber and no peak at 8.05 Å has been found. The difference with previous results [22] may be explained by the absence of Al in the preparation.

The large difference in the layer thickness of Fe-Hc (d = 7.48 Å) compared to Al-hemicarbonate ($3CaO \cdot Al_2O_3(CaCO_3)_{0.5}(CaO)_{0.5}12H_2O$) (d = 8.24 Å) indicates the presence of less water (and/or carbonate) in Fe-Hc than in Al-Hc. In the $CaO–Al_2O_3–CaCO_3–H_2O$ system, the Al-Hc appears first and then disappears with time to form Al-Mc [3,5]. Depending on the drying condition, the Al-Hc layer thickness may vary from 6.6 ($3CaO \cdot Al_2O_3(CaCO_3)_{0.5}(CaO)_{0.5}6.5H_2O$) to 8.2 Å ($3CaO \cdot Al_2O_3(CaCO_3)_{0.5}(CaO)_{0.5}12H_2O$) [23]. Based on the comparison with the Al system and on the TGA data after 180 days (Fig. 2) an interlayer water content of 3 to 4 H_2O could be roughly estimated for the Fe-Hc phase investigated. Thus we may suggest that the peak at 7.48 Å can be attributed to Fe-Hc with an amount of water close to 10: $3CaO \cdot Fe_2O_3(CaCO_3)_{0.5}(CaO)_{0.5}10H_2O$. However, the instability of this phase and its conversion to Fe-Mc does not permit a structural investigations and the carbonate and water content cannot be precisely determined. The formation of C_4FH_{13} would also have been possible, but again the measured interlayer thickness does fit neither the 7.94 Å reported for C_4AH_{13} nor the 7.35 Å reported for C_4AH_{11} [23]. In addition, the amount of calcite was clearly decreased after 180 days.

Table 1
Dissolution reaction used for thermodynamic calculation.

Phases	Reactions	log K_{So}	Ref
Al-ettringite	$Ca_6Al_2(SO_4)_3(OH)_{12}\cdot 26H_2O \rightarrow 6Ca^{2+} + 2Al(OH)_4^- + 3SO_4^{2-} + 4OH^- + 26H_2O$	−44.90	[a, c]
Fe-ettringite	$Ca_6Fe_2(SO_4)_3(OH)_{12}\cdot 26H_2O \rightarrow 6Ca^{2+} + 2Fe(OH)_4^- + 3SO_4^{2-} + 4OH^- + 26H_2O$	−44.00	[a, b]
Al-monosulphate	$Ca_4Al_2(SO_4)(OH)_{12}\cdot 6H_2O \rightarrow 4Ca^{2+} + 2Al(OH)_4^- + SO_4^{2-} + 4OH^- + 6H_2O$	−29.26	[a, c]
Fe-monosulphate	$Ca_4Fe_2(SO_4)(OH)_{12}\cdot 6H_2O \rightarrow 4Ca^{2+} + 2Fe(OH)_4^- + SO_4^{2-} + 4OH^- + 6H_2O$	−33.20	[a, b]
Al-monocarbonate	$Ca_4Al_2(CO_3)(OH)_{12}\cdot 5H_2O \rightarrow 4Ca^{2+} + 2Al(OH)_4^- + CO_3^{2-} + 4OH^- + 5H_2O$	−31.47	[a, c]
Fe-monocarbonate	$Ca_4Fe_2(CO_3)(OH)_{12}\cdot 6H_2O \rightarrow 4Ca^{2+} + 2Fe(OH)_4^- + CO_3^{2-} + 4OH^- + 6H_2O$	−34.59	[d]
Al-hemicarbonate	$Ca_4Al_2(CO_3)_{0.5}(OH)_{12}\cdot 6H_2O \rightarrow 4Ca^{2+} + 2Al(OH)_4^- + 0.5CO_3^{2-} + 5OH^- + 5.5H_2O$	−29.13	[a, c]
Fe-hemicarbonate	$Ca_4Fe_2(CO_3)_{0.5}(OH)_{12}\cdot 4H_2O \rightarrow 4Ca^{2+} + 2Fe(OH)_4^- + 0.5CO_3^{2-} + 5OH^- + 3.5H_2O$	−30.83	[d]
$Fe(OH)_3$ (am.)	$Fe(OH)_3(am) + OH^- \rightarrow Fe(OH)_4^-$	−2.60	[e]
$Fe(OH)_3$ (microcr.)	$Fe(OH)_3(Microcr)^- + OH^- \rightarrow Fe(OH)_4$	−4.10	[d]
$Al(OH)_3$ (am.)	$Al(OH)_3(amorphous)\ ^- + OH^- \rightarrow Al(OH)_4$	0.24	[a]
gibbsite	$Al(OH)_3(gibbsite)^- + OH^- \rightarrow Al(OH)_4$	−1.24	[e]
gypsum	$CaSO_4.2H_2O \rightarrow Ca^{2+} + SO_4^{2-} + 2H_2O$	−4.58	[e]
portlandite	$Ca(OH)_2 + 2\ H^+ \rightarrow Ca^{2+} + 2H_2O$	22.80	[e]
calcite	$CaCO_3 + H^+ \rightarrow Ca^{2+} + HCO_3^-$	1.85	[e]

[a] Lothenbach et al [6].
[b] Möschner et al [7].
[c] Matschei. et al [9].
[d] This study.
[e] GEMS/PSI TDB [15,17].

Fig. 2 shows the TGA curve caused by the loss of weight from the interlayer structure of Fe-Hc at different equilibration times. After 180 days equilibration the main loss of weight was between 110 and 180 °C, caused by the loss of 3–4 interlayer water from Fe-Hc. However, after 1 year equilibration, the loss of weight in the same temperature range was due to loss of water from both Fe-Hc and Fe-Mc.

3.2. Fe-monocarbonate

3.2.1. Kinetics of formation

Fig. 3 shows the XRD patterns of Fe-Mc at 20 °C as a function of equilibration time. The reaction of pure ferrite was slow and its counter was significantly lowered solely after 120 days. Both Fe-Mc and Fe-Hc were present after 120 days. However, after 3 years, only Fe-Mc was observed with some traces of calcite and portlandite. The latter sample was further used for the structural determination (solution and refinement) of Fe-Mc reported below. In the XRD patterns we also observed a shoulder at around 11.39° 2θ, which intensity decreased with drying. The synthesized solids had a slightly reddish color, which suggested the presence of small amounts of Fe-hydroxide not detectable by XRD.

C_4FH_{13} ($4CaO\cdot Fe_2O_3\cdot 13H_2O$) was not observed in any of the experiments. The presence of calcite destabilized the C_4FH_{13} phase, which led to the formation of carbonate containing Fe-AFm as previously reported [7,24]. This phenomenon was also observed for the Al analogues [9,25].

The thermogravimetric curve of Fe-Mc (Fig. 4) shows several mass losses between 80° and 800 °C. The first mass losses below 240 °C indicates the loss of the 6 waters from the interlayer of Fe-Mc as similarly observed for Al-Mc [26]. The water loss up to 500 °C is associated with the removal of the remaining 6 waters from the main layer and decomposition of traces of portlandite. The mass loss at about 700 °C is due to the loss of CO_2 from Fe-Mc and from calcite. The peak areas of calcite and portlandite were found to decrease with hydration time while Fe-Mc peaks increased. This finding further

Table 2
Thermodynamics data used for the calculation of the liquid phase compositions and for computation of thermodynamic parameters for the synthesized solids.

Phase	$\Delta_f G°$ [kJ/mol]	$\Delta_f H°$ [kJ/mol]	S^0 [J/mol.K]	$C^0{}_p$ [J/mol.K]	a_0 [J/mol.K]	a_1 [J/mol.K^2]	a_2 [J/mol.K]	a_3 [J/mol.K$^{0.5}$]	V^0 [cm^3/mol]	Ref.
Al-ettringite	−15,205.9	−17,535	1900	2174	1939	0.789	0	0	707	[a]
Fe-ettringite	−14,282.4	−16,600	1937	2200	1922	0.855	2.02e+06	0	717	[a,b]
Al-monosulphate	−7778.5	−8750	821	942	594	1.168	0	0	309	[a, c]
Fe-monosulphate	−6882.6	−7843	858	968	577	1.234	2.02e+06	0	322	[a, b]
Al-monocarbonate	−7337.5	−8250	657	881	618	0.982	−2.59e+06	0	262	[a, c]
Fe-monocarbonate	−6674.0	−7485	1230	950	612	1.160	−5.73e+05	0	292	[d]
Al-hemicarbonate	−7336.0	−8270	713	906	664	1.014	−1.30e+06	−800	285	[a, c]
Fe-hemicarbonate	−5952.9	−6581	1270	841	308	1.200	−9.08e+05	3200	273	[d]
$Al(OH)_3$ (am.)	−1143.2	−1281	70	93	36	0.191				[e]
gibbsite	−1150.9	−1289	70	93	36	0.191			32	[e]
$Fe(OH)_3$ (am.)	−700.2	−879	88	43	28	0.052	0	0	34	[e]
$Fe(OH)_3$ (microcr.)	−708.8	−841	88	43	28	0.052	0	0	34	[d]
gypsum	−1797.8	−2023	194	186	91	0.318	0	0	75	[e]
portlandite	−897.0	−985	83	88	187	−0.022	0	−1600	33	[e]
calcite	−1129.2	−1207	93	82	105	0.022	−2.59e+05	0	37	[e]
CaO	−604.0	−635	40	43	49	0.004	−6.53e+05	0	17	[e]
Al_2O_3	−1568.3	−1662	51	79	115	0.018	−3.51e+06	0	26	[e]
Fe_2O_3	−8214.0	−8214	88	105	98	0.078	−1.49e+06	0	30	[e]

[a] Lothenbach et al [6].
[b] Möschner et al [7].
[c] Matschei. et al [9].
[d] This study.
[e] Thoenen et al and Hummel et al [16,17].

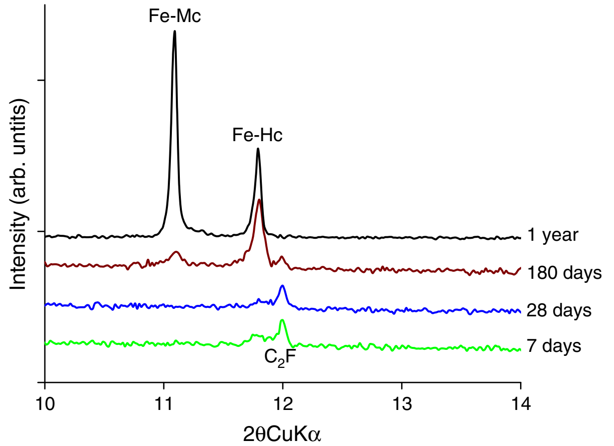

Fig. 1. Time-dependent XRD pattern of Fe-Hc (and Fe-Mc) synthesized at 20 °C; C_2F: $2CaO\cdot Fe_2O_3$, Fe-Mc: Fe-monocarbonate, Fe-Hc: Fe-hemicarbonate.

substantiates that the formation of synthetic Fe-Mc was completed after long hydration times.

3.2.2. Structure of Fe-Mc

The virtually single phase (absence of Fe-Hc phase) Fe-Mc sample obtained after 3 years reaction time was subject to crystallographic structure determination using synchrotron powder XRD. High quality diffraction data allowed the structure of Fe-Mc to be solved and refined. The sample was composed of 89 wt.% (weight percent) of the studied Fe-Mc phase with some impurities of calcite (11 wt.%). The crystal data and multi-pattern refinement (using data from two samples to detector distances) parameters are summarized in Table 3 while a Rietveld plot (corresponding to data from the sample to detector distance of 150 mm) is shown in Fig. 5.

Fe-Mc was found to crystallise in the rhombohedral $R\overline{3}c$ space group, i.e. the highest symmetry observed for AFm phases, which further corresponds to the symmetry of the high temperature (HT)-polymorph of Friedel's salt [27,28]. The structure is composed of a positively charged main layer $[Ca_2Fe(OH)_6]^+$ and a negatively charged interlayer $[1/2CO_3\cdot 3.10(2)H_2O]^-$. The main layer contains trivalent Fe^{3+} cations in hydroxide octahedral coordination (i.e. substituting Al^{3+} cations usually encountered in AFm phases) and bivalent Ca^{2+} cations, which are seven-fold coordinated (6 hydroxyls + 1 water molecule from interlayer). The structure of Fe-Mc was described by 7 non-H atomic positions: one atomic position for iron, for calcium, for hydroxyl ions, for water molecule bonded to Ca^{2+} (labelled Ow1), for water molecule weakly bonded in the centre of the interlayer (labelled Ow2 with a refined partial occupancy of 0.36), for carbon atom from carbonate group (with a fixed partial occupancy of 1/2 in agreement with the electroneutrality of the compound) and for oxygen atoms from carbonate (labelled Oc). The interlayer was described in terms of a statistic distribution between one carbonate group and two water molecules. The refined composition was very close to $3CaO\cdot Fe_2O_3\cdot CaCO_3\cdot 12H_2O$, which is the composition determined by TGA. Atomic coordinates of the 7 crystallographic sites are indicated in Table 4, whereas interatomic distances are given in Table 5.

The accuracy of the refined structural model is reflected by the refined values for the interatomic distances in the main layer and the interlayer. The only unrealistic Ow2–Ow2 distance of 2.208 Å is attributed to partial occupancies in this region of the structure: one carbonate anion is statistically distributed with two water molecules in the location at the centre of interlayer. An equivalent situation (statistical distribution between one carbonate group and three water molecules) was described earlier in the case of the disordered $D-C_4A\overline{C}H_{11}$ structure [29]. The structure of Fe-Mc is presented in Fig. 6, showing a general representation (Fig. 6A) and details of the network of hydrogen bonding assuming the cohesion between main and interlayer (Fig. 6B).

Extended X-ray absorption fine structure (EXAFS) spectroscopy was carried out to determine the local arrangement of Fe in Fe-Mc. Synchrotron-based X-ray absorption spectroscopy is a local probing technique, which provides information on the coordination environment of the X-ray absorbing atom within a distance of up to ~5 Å. Experimental and theoretical Fourier transforms (modulus) obtained from the spectrum are shown in Fig. 7 while the structural parameters are summarized in Table 6. The central atom Fe has six neighboring O atoms at a distance of 2.02 Å and six neighboring Ca atoms at 3.47 Å. The former finding confirms that Fe is octahedrally coordinated in Fe-Mc. Furthermore, the Fe–O and Fe–Ca distance agrees with the refined XRD data (2.04 and 3.46 Å respectively). Absence of any Fe–Fe backscattering contributions, which are expected at 3.01 Å [7,30], suggested that, if at all, Fe-hydroxide was present in the 3 years old sample below the detection limit of the method (~5 wt.%).

Raman spectra from Fe-Mc confirmed the refined structure of Fe-Mc, namely the interlayer description (Fig. 8). The symmetric stretching band of carbonate $[CO_3]$ groups was observed at 1085 cm^{-1} (Fig. 8A). In

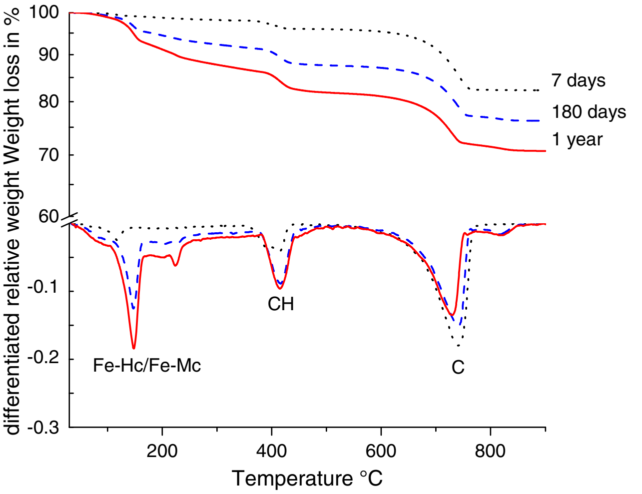

Fig. 2. TGA and DTG curves of Fe-Hc formation at 20 °C for different equilibration times. CH: Portlandite, C: carbonates.

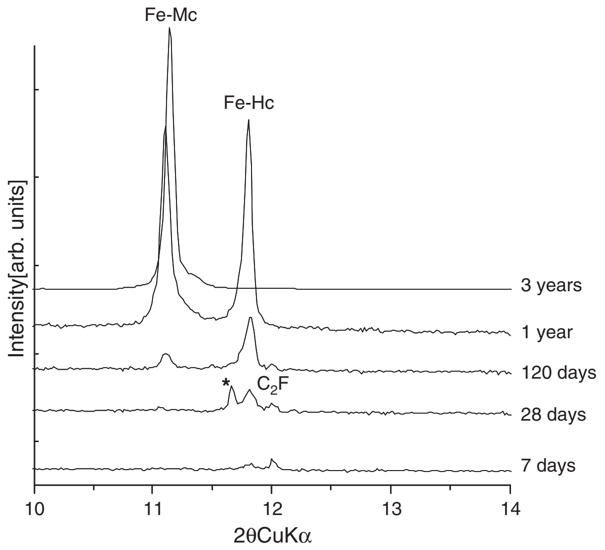

Fig. 3. Time-dependent XRD pattern of Fe-Mc formed at 20 °C. * unidentified peak.

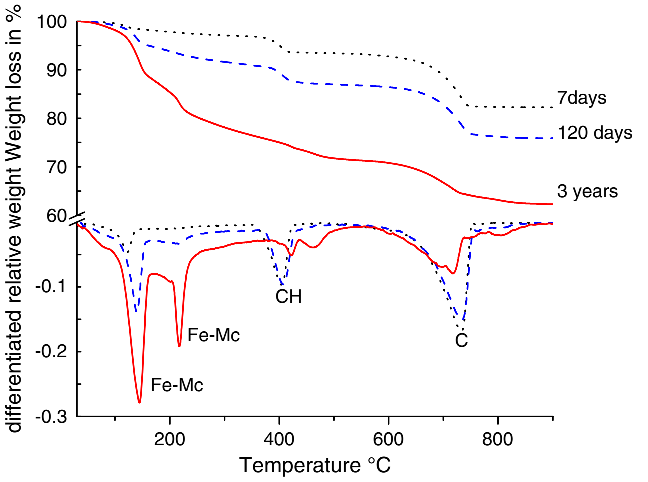

Fig. 4. TGA and DTG curves of Fe-Mc formation at 20 °C for different equilibration times. CH: Portlandite, C: carbonates.

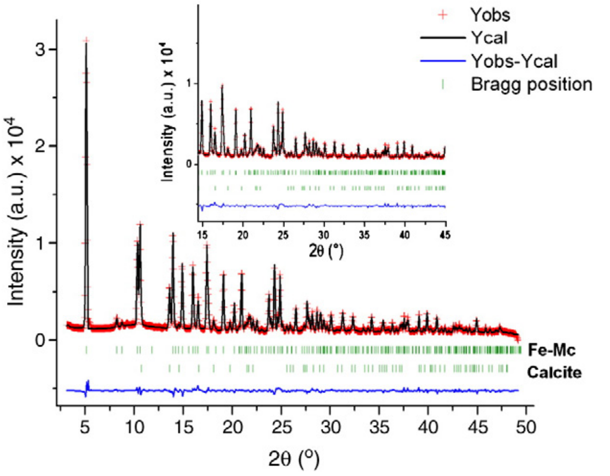

Fig. 5. Rietveld plot from powder pattern recorded with a sample-to-detector distance of 150 mm (red crosses are experimental data, black line is calculated pattern, blue line is the difference pattern, green sticks are Bragg peaks positions for Fe-Mc and calcite).

a recent study the 1085 cm^{-1} value for the carbonate ν_1 mode was attributed to carbonate weakly bonded at the centre of interlayer [31,32]. This mode of vibration is clearly shifted from 1068 cm^{-1} as observed in the case of carbonate bonded to the main layer of, for example, Al-Mc. The broad and unresolved band of vibration observed in the frequency range 2800 cm^{-1}– 4000 cm^{-1} characterizes a disordered interlayer region (Fig. 8B). The hydrogen bond network is not well defined neither in space due to statistic disorder nor in time due to dynamical disorder (libration of carbonate group around the trigonal axis and/or movement of weakly bonded Ow2 water molecules). The latter observations have been reported for AFm phases [33,34].

ESEM micrograph of the synthesized solids also show a platey crystals with hexagonal symmetry as shown in Fig. 9, which indicates a preferred orientation of the crystals formed. This agrees with the platey crystals of Al-containing AFm phases [23,35].

3.2.3. Comparison of pure Fe- and Al-Mc

The Fe-Mc and analogous Al-Mc compounds exhibit different symmetries. The Fe-Mc structure is represented by the highly symmetric $R\overline{3}c$ space group whereas the Al-Mc structure is described by the triclinic symmetry, one ordered structure described in the $P1$ space group [1] and one disordered structure in the $P\overline{1}$ space group [29]. The two monocarbonate analogues have different layer spacing: about 7.98 Å for Fe-Mc, and about 7.57 Å for Al-Mc. This difference is attributed to the location of carbonate anions. CO_3^{2-} anions are bonded to the main layer in Al-Mc as one of the three oxygen atoms of the carbonate group occupies the seventh coordination position of a seven fold coordinated Ca^{2+} cation from the main layer. In the case of Fe-Mc, however, carbonate anions are located in the centre of the interlayer, weakly bonded via hydrogen bonds in a position parallel with the main layer (see Fig. 6). Such pronounced differences in symmetry and carbonate locations are expected to be incompatible with the existence of a complete solid solution series expressed by $Ca_4[(Al_xFe_{1-x})_2(OH)_{12}].CO_3.(6-x)H_2O$.

The unit cell parameter *a* of Fe-Mc is at 5.92 Å somewhat larger than for Al-Mc (*a* = 5.78 Å) due to the larger ion radius of iron (0.64 Å) compared to aluminium (0.51 Å) [36].

In Fig. 10 the results of TGA and DTG analysis of Al-Mc and Fe-Mc are shown, which allow the following steps to be distinguished:

$$Ca_4[(Al_xFe_{1-x})_2(OH)_{12}].CO_3.5\text{–}6H_2O \rightarrow Ca_4[(Al_xFe_{1-x})_2(OH)_{12}].CO_3 + 5\text{–}6H_2O\ \text{(interlayer water removal)}$$

$$Ca_4[(Al_xFe_{2-x})(OH)_{12}].CO_3 \rightarrow Ca_4[(Al_xFe_{1-x})_2O_6].CO_3 + 6H_2O\ \text{(dehydroxylation)}$$

$$Ca_4[(Al_xFe_{2-x})O_6].CO_3 \rightarrow Ca_4[(Al_xFe_{1-x})_2O_7] + CO_2\ \text{(decarbonation)}$$

From the TGA analysis the interlayer water of Fe-Mc was calculated and the number of interlayer water molecules per unit cell was found to be approximately 5.8 resulting in total water content of 11.8. By heating $Ca_3[Fe_2(OH)_6]_2 \cdot CaCO_3 \cdot 6H_2O$, all the molecules of

Table 3

Multi pattern refinement (from two sample-to-detector distances: 1/150 mm, and 2/350 mm) and crystal data of Fe-Mc.

Compound	Iron monocarbonate
Formula	$3CaO \cdot Fe_2O_3 \cdot CaCO_3 \cdot 12.18(4)H_2O$
Structural formula	$[Ca_2Fe(OH)_6]^+[1/2CO_3 \cdot 3.10(2)H_2O]^-$
Calculated formula weight (g mol^{-1})	646.91
T(K)	293 K
System	Rhombohedral
Space group	$R\overline{3}c$
a (Å)	5.9196 (1)
c (Å)	47.8796 (10)
V ($Å^3$)	1453.01 (4)
Z/Dx (g cm^{-3})	6/2.22
Wavelength (Å)1	0.720852
Angular range 2θ (°) 1, 2	3.14–49.16, 2.50–26.35
Nobs 1, 2	1283, 1111
Excluded regions (°)	5.40–5.61 and 9.03–9.71
Nref 1, 2	288, 52
Rp 1, 2 (%)	3.27, 3.89
Rwp 1, 2 (%)	4.40, 5.37
RBragg 1, 2(%)	4.38, 3.43
RF 1, 2 (%)	4.73, 3.31
N of profile parameters	20
N intensity dependent parameters	15

Table 4

Fractional coordinate of non hydrogen atoms and isotropic displacement.

Atom	Site	x	y	z	Ueq × 10^3 (A^2)	Occ
Fe	6*b*	0	0	0	9.6 (8)	1.000
Ca	12*c*	1/3	2/3	0.01134 (4)	8.3 (8)	1.000
OH	36*f*	0.3863 (6)	0.4006 (5)	0.1447 (1)	1.7 (1)	1.000
Ow1	12*c*	1/3	2/3	0.0635 (1)	36 (2)	1.000
C	6*a*	0	0	1/4	65 (5)	0.5(−)
Oc	18*e*	0	-0.2153(9)	1/4	= Ueq (C)	0.5(−)
Ow2	18*e*	0	= y (Oc)	1/4	= Ueq (C)	0.368(8)

Table 5
Selected interatomic distances (Å) in Fe-Mc.

Atom	Atom	Distances (Å)
Fe	6 × OH	2.043(5)
Ca	3 × OH	2.385 (8)
	3 × OH	2.472 (8)
	Ow1	2.50 (1)
C	3 × Oc	1.275 (1)
Ow1	1/2 (3 × Oc)	2.58 (2)
	1/2 (2 × Ow2)	2.58 (2)
(Oc,Ow2)	2 × Ow1	2.58 (2)
	2 × OH	3.273 (1)
	2 × OH	3.50 (1)
Ow2	Ow2	“2.208 (1)”

water from the interlayer were driven off around 240 °C which agrees with the findings of Ecker et al. [24] and with the amount of interlayer water determined by XRD. The weight loss up to 500 °C indicates the dehydroxylation of the water associated with the main layer and traces of portlandite. Finally the weight loss around 700 °C represents decarbonation of calcite and Fe-Mc. The interlayer water of $Ca_3[Al_2(OH)_6]_2.CaCO_3.5H_2O$ was removed at somewhat lower temperatures than in the case of Fe-Mc, i.e. in the range between 80 and 270 °C in several steps. The interlayer water of Al-Mc was found to be around 5.2.

The IR results of Fe-Mc and Al-Mc are summarized in Fig. 11 and Table 7. The IR spectra of Fe-Mc are correlated with the Al-analogues spectra to assign the type of bonds at different absorption bands and compared with the study from Ecker et al. [24]. The IR spectra of Al-Mc have been assigned based on the study of Fischer et al. [23] and Trezza et al. [37]. The IR frequency at 670 cm^{-1}, 817 cm^{-1} and 952 cm^{-1} is due to the vibrations of the AlO_6 bond in the main layer. The strong IR frequencies at 1360 cm^{-1} and 1415 cm^{-1} are bands attributed to the asymmetric stretching vibration of ν_3-CO_3^{2-} while the sharp peak at 880 cm^{-1} is related to the bending vibration of ν_2-CO_3^{2-}. The absorption band in the range between 3000 cm^{-1} and 3600 cm^{-1} is due to OH stretching vibrations resulting from the interlayer water. In the case of Fe-Mc the weak bands at 661 cm^{-1} and 960 cm^{-1} are attributed to FeO_6 vibrations. Like the Al-analogues, ν_2-CO_3^{2-} vibration in Fe-Mc spectra is assigned at 875 cm^{-1}. The sharp band at 1382 cm^{-1} is related to the vibration of ν_3-CO_3^{2-}. The broad band between 2700 cm^{-1} and 3320 cm^{-1} is due to the vibration of OH bond in the interlayer water of Fe-Mc. The bands at frequencies higher than 3600 cm^{-1} can be related to the vibrations of OH in the main layer $[Ca_2.(Al,Fe)(OH)_{12}]^+$. The peaks of Al-Mc are sharper between 3000 cm^{-1} and 3600 cm^{-1} than those of Fe-Mc indicating more highly coordinated interlayer water in Al-Mc.

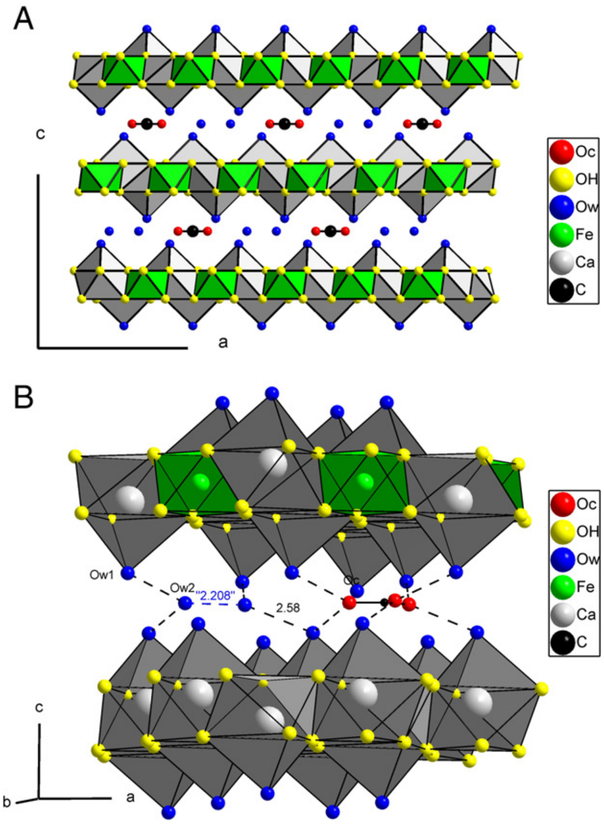

Fig. 6. A. Projection of the Fe-Mc structure along *b* axis (the interlayer part of the structure is ordered for clarity; i.e. the statistical distribution between one carbonate and two water molecule has been alternatively ordered). B. 3D cohesion in Fe-Mc structure (representation of the main hydrogen bonds).

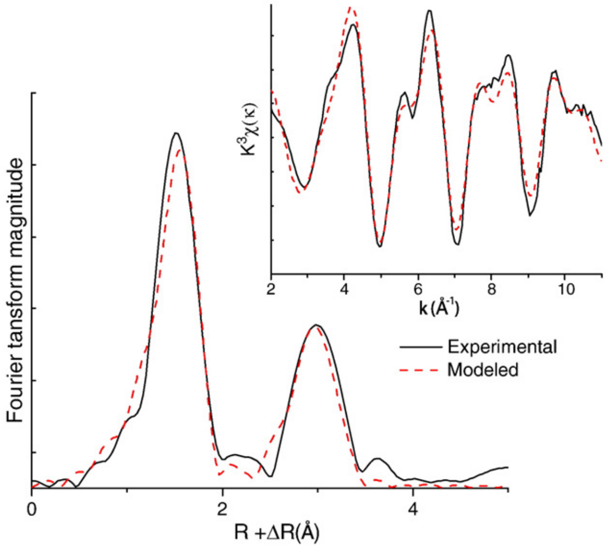

Fig. 7. Fe K-edge EXAFS data of Fe-Mc: Experimental (solid line) and theoretical (dots) Fourier transform (modulus) obtained from k^3-weighted, normalized, background-subtracted spectrum (inset).

3.2.4. Mixed $3CaO·(Al_xFe_{1-x})_2O_3·CaCO_3·nH_2O$ systems

Variations of the Al/Fe ratio in the $3CaO·Al_2O_3·CaCO_3·11H_2O$ — $3CaO·Fe_2O_3·CaCO_3·12H_2O$ system resulted in the formation of two separate stable phases (no systematic peak shifts) while no intermediate phase formed (Fig. 12). The intensity of the small intermediate peak at 11.39° 2θ depended on the water content and decreased upon drying. To index the reflections and to determine the layer thickness and the unit cell parameter *a*, a Le Bail fitting was performed. The results are shown in Figs. 13 and 14, respectively. No significant variation of both parameters with varying Al mol fraction

Table 6
EXAFS structural parameters of Fe-Mc equilibrated for three years.

Atomic pair	N	R(Å)	R(Å) from XRD	σ^2(Å^2)	ΔE_0 (eV)	R-factor
Fe-O	6.0[a]	2.02	2.04	0.006	1.18	0.056
Fe-Ca	6.0[a]	3.47	3.46	0.008	1.18	

N: Coordination number of the neighboring atom (uncertainty ± 20%).
R: distance to the neighboring atom (uncertainty ± 0.020 Å).
σ: Debye–Waller factor.
ΔE_0: inner potential correction.
R-factor: deviation between experimental data and fit.
[a] Fixed parameter.

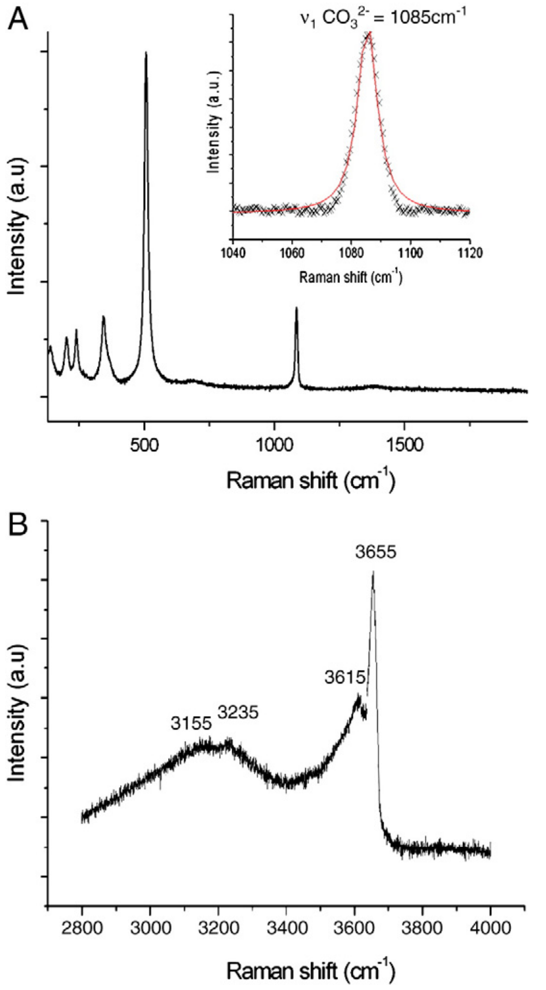

Fig. 8. A. Raman spectra on Fe-Mc in the frequencies range 200 cm^{-1}–1800 cm^{-1}. B. Raman spectra on Fe-Mc in the frequencies range 2800 cm^{-1}–4000 cm^{-1}.

was observed compared to end member values. These results clearly confirm the absence of a solid solution between Al-Mc and Fe-Mc, in contrast to the findings reported elsewhere [22]. Thus, comparison of the XRD pattern further corroborated that $3CaO·Al_2O_3·CaCO_3·11H_2O$ and $3CaO·Fe_2O_3·CaCO_3·12H_2O$ have different symmetries in their structure, different carbonate location and different amounts of water in the interlayer.

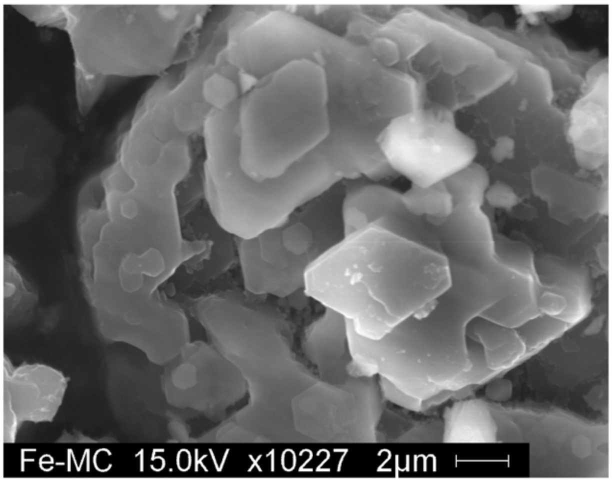

Fig. 9. The ESEM micrographs of Fe-Mc.

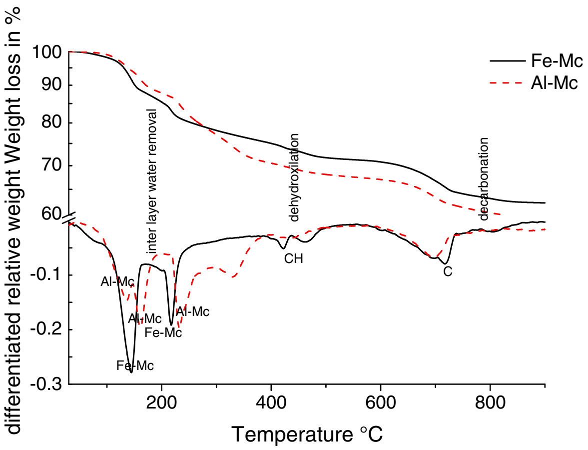

Fig. 10. Thermal analysis (DTG and TGA) of $Ca_3(Al_xFe_{1-x})_2O_3.CaCO_3.nH_2O$.

3.2.5. Effect of temperature

X-ray diffraction and the TGA measurements revealed that the formation of Fe-Hc and Fe-Mc was faster at 50 °C (Table 8). First indications of the formation of Fe-Mc were observed after 7 days of equilibration. The TGA and XRD data further revealed that after 28 days and longer the intensities of portlandite and calcite increased while the peaks of Fe-Mc decreased suggesting instability of Fe-Mc with regard to calcite, portlandite and Fe-hydroxide at higher temperature and longer equilibration time. At 50 and 80 °C the diffraction pattern also indicated the presence of hematite (Fe_2O_3) (see Fig. 15). At 80 °C, neither Fe-Hc nor Fe-Mc was observed, hematite, calcite and portlandite were the only phases identified. The color of the solid formed was dark red, thus confirming the presence of Fe-oxide or hydroxide [7]. The findings showed that Fe-Mc is unstable at 80 °C and decomposes to Fe_2O_3, calcite and portlandite.

4. Solubility

The composition of the solutions in equilibrium with pure Al-Mc, Fe-Mc, Fe-Hc and mixtures were determined at different equilibration times and at 20 °C and 50 °C (Tables 8 and 9). The very low Fe concentrations detected in solution indicated the presence of an additional phase, presumably Fe-hydroxide. Note that the presence of Fe-hydroxide is consistent with the slightly red colouring of the samples.

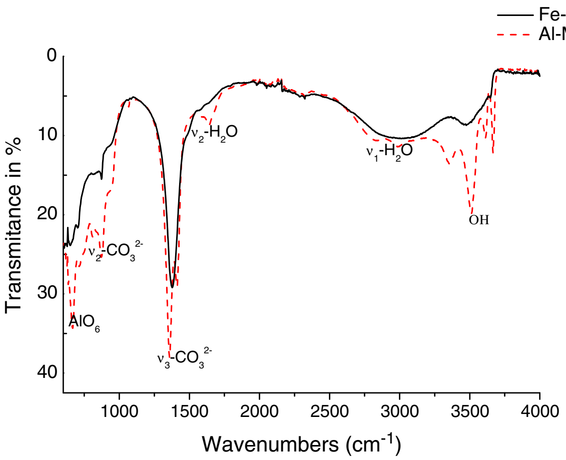

Fig. 11. IR spectra of Al-Mc and Fe-Mc.

Table 7
IR vibrations of $Ca_4[(Al_xFe_{1-x})_2(OH)_{12}].CO_3.nH_2O$.

Al-Mc		Fe-Mc	
Wavenumbers (cm^{-1})	Vibrations	Wavenumbers (cm^{-1})	Vibrations
670	AlO_6	661	FeO_6
720	ν_4-CO_3^{2-}	710	ν_4-CO_3^{2-}
817	AlO_6		
880	ν_2-CO_3^{2-}	875	ν_2-CO_3^{2-}
952	AlO_6	960	FeO_6
1360	ν_3-CO_3^{2-}	1382	ν_3-CO_3^{2-}
1415	ν_3-CO_3^{2-}		
1651	ν_2-H_2O		
3007	ν_1-H_2O		
3369	ν_1-H_2O	2700–3320	ν_1-H_2O
3518	OH^-	3505	OH^-
3616	OH^-[a]		
3668	OH^-[a]	3653	OH^-[a]

[a] Associated to the main layer.

4.1. Determination of solubility products at 20 °C and 50 °C

The measured concentrations of calcium, hydroxide, aluminium and iron were used to calculate the solubility products using GEMS:

$$K_{S0\ Al-monocarbonate} = \left\{Ca^{2+}\right\}^4 \cdot \left\{Al(OH)_4^-\right\}^2 \cdot \left\{CO_3^{2-}\right\} \cdot \left\{OH^-\right\}^4 \cdot \left\{H_2O\right\}^5 \tag{6}$$

$$K_{S0,Fe-monocarbonate} = \left\{Ca^{2+}\right\}^4 \cdot \left\{Fe(OH)_4^-\right\}^2 \left\{CO_3^{2-}\right\} \cdot \left\{OH^-\right\}^4 \cdot \left\{H_2O\right\}^6 \tag{7}$$

$$K_{S0,Fe-hemicarbonate} = \left\{Ca^{2+}\right\}^4 \cdot \left\{Fe(OH)_4^-\right\}^2 \cdot \left\{CO_3^{2-}\right\}^{0.5} \left\{OH^-\right\}^5 \cdot \left\{H_2O\right\}^{3.5} \tag{8}$$

where {} denotes the activity.

As dissolved carbonate, CO_3^{2-}, could not be measured reliably, the concentration of CO_3^{2-} was calculated based on the assumption that all solutions were in equilibrium with solid calcite. The calculated solubility products are listed in Tables 8 and 9. From the calculated total solubility products, the Gibbs free energy of the reaction, $\Delta_{r,T}G^0$ at a temperature T was computed according to Eq. (9):

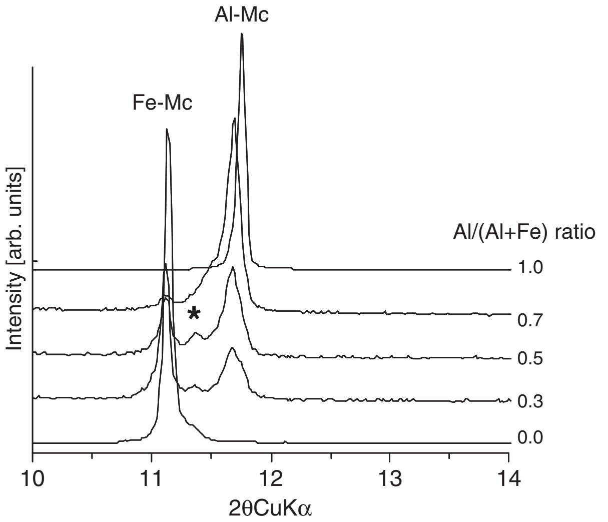

Fig. 12. XRD pattern of the Al/Fe-Mc after 3 years hydration time at 20 °C * peak due to additional water in Mc.

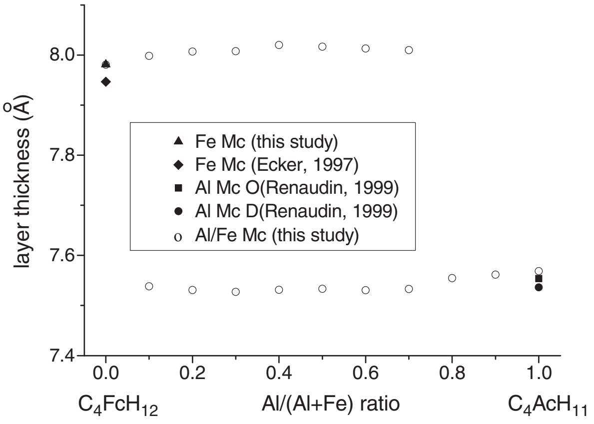

Fig. 13. Layer thickness for Al-Mc and Fe-Mc after refinement by Le Bail fitting and Rietveld analysis. C_4FcH_{12}: Fe-Mc, C_4AcH_{11}: Al-Mc.

$$\Delta_{r,T}G^0 = -RT\ lnK_{S0,T} \tag{9}$$

where R = 8.31451 J/(molK) is the universal gas constant and T the temperature T in Kelvin.

The total solubility products at 20 °C were determined to be log $K_{S0\ Al-Mc} = -31.55$, log $K_{S0\ Fe-Mc} = -34.51 \pm 0.50$ and log $K_{S0\ Fe-Hc} = -30.55 \pm 0.67$. The value determined for Al-Mc at 20 °C is nearly identical to the value of −31.47 reported by Matschei et al. [9] at 25 °C. Möschner et al. [7] reported a tentative solubility product of −35.9 for Fe-Mc at 20 °C, which is one log units lower than the value determined in this study.

At 50 °C a solubility product of log $K_{S0} = -35.27 \pm 0.17$ was determined for Fe-Mc and a log $K_{S0} = -32.58 \pm 0.61$ for Fe-Hc. Thus, the solubility products at 50 °C are lower than those determined at 20 °C. Even though Fe-Mc was stabilized at 50 °C, the phase becomes unstable with time with respect to Fe-hydroxide, calcite and portlandite. At 80 °C both Fe-Mc and Fe-Hc were found to be unstable with respect to calcite and hematite (Fe_2O_3). Additionally, the solutions equilibrated at 20 °C and 50 °C were thermodynamically oversaturated with respect to Fe-hydroxide and hematite. The kinetics of formation of hematite, however, was very slow, so that the solid did not form at 20 °C or 50 °C within the experimental period.

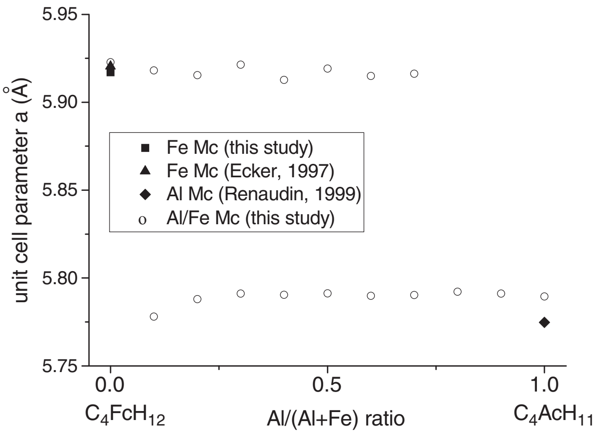

Fig. 14. Values of a-parameters for Al-Mc and Fe-Mc.

Table 8
Measured ion concentrations and calculated solubility products at different equilibration times.

Equilibration time in days	Temperature	Ca(mmol/l)	Al(mmol/l)	Fe(mmol/l)	K(mmol/l)	pH	Solid phases present	logKsp Fe-Mc	logKsp Fe-Hc	logKsp Al-Mc
Fe-Hc										
7	20	5.18	<0.003	0.002	91	12.95	Fe-Mc,Fe-Hc,**C,P**		−30.11	
28	20	4.92	<0.003	0.004	90	12.85	Fe-Mc,Fe-Hc,**C,P**		−30.14	
180	20	4.56	<0.003	0.002	90	12.98	Fe-Mc,**Fe-Hc**,C,P		−30.40	
400	20	5.83	<0.003	0.002	90	13.00	**Fe-Mc,Fe-Hc**,C,P		−30.01	
Fe-Mc										
7	20	5.79	<0.003	0.0060	98	13.01	Fe-Mc,Fe-Hc,**C,P**	*−31.93*	−30.16	
28	20	5.36	<0.003	0.0007	99	13.05	Fe-Mc,Fe-Hc,**C,P**	*−33.94*	−30.52	
370	20	5.40	<0.003	0.0013	88	12.99	**Fe-Mc,Fe-Hc**,C,P	*−33.46*	−32.11	
1100	20	3.77	<0.003	0.0004	89	13.06	**Fe-Mc**, C, P	−34.98		
7	50	5.02	<0.003	0.0050	98	13.04	Fe-Mc,**Fe-Hc,C,P**	*−34.10*	−31.90	
28	50	3.62	<0.003	0.0025	96	13.03	**Fe-Mc**,Fe-Hc,C,P	−35.16	−33.03	
120	50	5.00	<0.003	0.0050	n.d	12.79	**Fe-Mc**,Fe-Hc,C,P	−35.19	−32.08	
370	50	4.50	<0.003	0.0013	91	12.99	**Fe-Mc**, Fe-Hc,C, P,Fe2O3	−35.47	−33.31	
Al-Mc										
1100	20	0.12	2.08	<0.0001	94	13.02	**Al-Mc**, C			−32.14
Fe-Mc	**20**	mean of all solid solution experiments supersaturation (Table 9)						**−34.83 ± 0.50**		
Fe-Mc	**20**	mean of all solid solution experiments undersaturation (Table 9)						**−34.19 ± 0.50**		
		mean of supersaturation and undersaturation						**−34.51 ± 0.50**		
Fe-Mc	**50**	mean of values ≥28 days						**−35.27 ± 0.17**		
Fe-Hc	**20**	mean of all values							**−30.55 ± 0.67**	
Fe-Hc	**50**	mean of all values							**−32.58 ± 0.61**	
Al-Mc	**20**	mean of all solid solution experiments at 1100 days (Table 9)								**−31.55 ± 0.29**

Detection limits (mmol/L): Al = 0.003, Ca = 0.02, Fe = 0.00009, K = 0.04. Bold: Main phase.

For Al-Mc and Al-Hc, an increase in the solubility with increasing temperatures was observed [9], while in contrast, for both Fe-Hc and Fe-Mc a slight decrease was observed suggesting a slight stabilization of Fe-Hc and Fe-Mc (Fig. 16).

4.2. Estimation of the solubility product under standard conditions

The solubility products at standard conditions was calculated with the help of GEMS-PSI using temperature extrapolation from the solubility products calculated at 20 °C and 50 °C as previously demonstrated by Matschei et al. [2]. The calculated solubility products at 20 °C and 50 °C (Tables 8 and 9) were used to develop the temperature-dependent 'log K' function which allowed the solubility products to be calculated at different temperatures (Fig. 16) as described in Section 2.3. The entropy was adjusted until good agreement between measured and calculated solubility was reached. The thermodynamic properties of the solids at 25 °C are listed in Table 10. The solubility product of Fe-Mc (-34.59) is about 2-3 log units lower than that of Al-Mc (-31.47). Note that a similar difference in the solubility product between Al- and Fe-monosulphate was found (Table 1), while the solubility product of Fe-ettringite (−44.0) was found to be slightly higher than that of Al-ettringite (−44.9). This indicates that the Fe-AFm phases are potentially stable under conditions where Al-AFm can be formed while the formation of Fe-ettringite is less probable under conditions where Al-ettringite is stable.

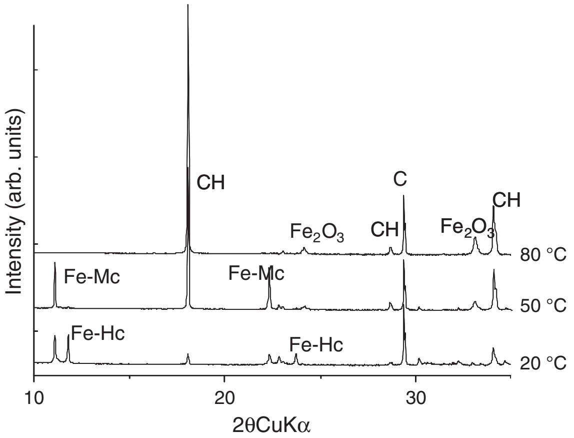

Fig. 15. Comparison of XRD pattern of Fe-Mc equilibrated for one year at 20, 50 and 80 °C. CH: portlandite, C: carbonate, Fe_2O_3: hematite.

4.3. Mixed $3CaO\cdot(Al_xFe_{1-x})_2O_3\cdot CaCO_3\cdot nH_2O$ systems

Table 9 shows the compositions of the liquid phase with varying the Al mole fraction. The concentrations of all the species (Ca, Al, Fe, K) between 0.1 and 0.9 mole fraction of Al in the $3CaO(Al_xFe_{1-x})_2O_3\cdot CaCO_3\cdot nH_2O$ system were found to be similar within the uncertainty range, indicating the presence of two separate solid phases (Table 9). Fig.17 shows that the calculated and measured concentrations are comparable on the assumption that two separate phases are present. This supports the findings from XRD, that showed no solid solution between the Al- and Fe-Mc end members. Note that the presence of a solid solution would be indicated by gradual changes in the elemental concentrations (see dotted line in Fig. 17).

5. Modelling of C_3A–C_2F–$CaCO_3$–$CaSO_4$–H_2O system in cement hydration

Thermodynamic modelling was used to calculate the changes of the hydrate assemblage in the system C_3A–C_2F–$CaCO_3$–$CaSO_4$–H_2O ($SO_3/(Al,Fe)_2O_3 = 1$) in the absence and presence of $CaCO_3$ using the thermodynamic data given in Tables 1 and 2 with the aim of assessing differences in the properties of Fe-and Al-analogues and the effect of calcite. The model calculations used a fixed $SO_3/(Al,Fe)_2O_3$ ratio of 1 and varied the calcite content ($CO_2/(Al,Fe)_2O_3$ ratio). A constant amount of solids ($Al_2O_3 + Fe_2O_3 + CaSO_4 + CaO + CaCO_3$) was maintained.

Table 9
Compositions of Al/Fe-monocarbonate after synthesis at 20 °C equilibrated for 3 years in supersaturated and undersaturated condition.

Mole fraction of Al in the solids	Al(mmol/L)	Ca(mmol/L)	Fe(mmol/L	K(mmol/L)	pH	Solids present	logKso Al-Mc	logKso, Fe-Mc
Supersaturation								
1	2.08	0.12	<0.0001	94	13.02	Al-Mc. C	−32.14	
0.9	0.02	3.59	0.0004	92	12.97	Al-Mc,Fe-Mc	−31.68	−35.05
0.8	0.02	3.72	0.0004	92	12.99	Al-Mc,Fe-Mc	−31.46	−34.98
0.7	0.03	3.72	0.0004	91	12.95	Al-Mc,Fe-Mc	−31.27	−34.98
0.6	0.03	3.79	0.0003	91	12.97	Al-Mc,Fe-Mc	−31.26	−35.21
0.5	0.03	3.74	0.0005	91	12.95	Al-Mc,Fe-Mc	−31.32	−34.78
0.4	0.03	3.74	0.0008	90	12.97	Al-Mc,Fe-Mc	−31.37	−34.37
0.3	0.02	3.72	0.002	79	12.95	Al-Mc,Fe-Mc	−31.41	−33.59
0.2	0.02	3.19	0.0004	90	12.95	Al-Mc,Fe-Mc	−31.89	−35.3
0.1	0.02	3.64	0.0004	89	12.97	Al-Mc,Fe-Mc	−31.65	−35.02
0	<0.003	3.77	0.0004	89	13.06	Fe-Mc, C, P		−34.98
						Average	−31. 55 ± 0.29	−34.83 ± 0.50
Undersaturation								
1	n.d	1.77	0.0017	88	13.03	Al-Mc, C	n.d	
0.9	n.d	2.72	0.0019	94	13.03	Al-Mc,Fe-Mc, C	n.d	−34.05
0.8	n.d	1.81	0.0088	90	13.01	Al-Mc,Fe-Mc, C	n.d	−33.31
0.7	n.d	2.05	0.0014	89	13.01	Al-Mc,Fe-Mc, C	n.d	−34.74
0.6	n.d	3.29	0.0012	90	13.01	Al-Mc,Fe-Mc, C	n.d	−34.22
0.5	n.d	2.17	0.0012	90	13.01	Al-Mc,Fe-Mc, C	n.d	−34.79
0.4	n.d	3.47	0.0009	93	13.01	Al-Mc,Fe-Mc, C	n.d	−34.38
0.3	n.d	3.20	0.0012	89	13.01	Al-Mc,Fe-Mc, C	n.d	−34.28
0.2	n.d	4.02	0.0016	88	13.01	Al-Mc,Fe-Mc, C	n.d	−33.72
0.1	n.d	2.42	0.0011	90	13.03	Al-Mc,Fe-Mc, C	n.d	−34.71
0	n.d	5.47	0.0009	88	13.03	Fe-Mc, C, P		−33.68
						Average		−34.19 ± 0.50

Detection limit (mmol/l): Al = 0.003 Ca = 0.02, Fe = 0.00009, K = 0.04; measurement uncertainity ± 5%.

In the absence of calcite, Al- and Fe-monosulphate (Ms) were calculated to be stable in presence of small amounts of portlandite (Fig. 18). Upon sequential addition of calcite, first Fe-Hc and Al-ettringite are expected to form at the expense of Al- and Fe-Ms. Appearance of Al-Hc, Fe-Mc and finally Al-Mc occurs with increasing supply of carbonate. The influence of calcite on the composition of the phase assemblage of a hydrated model Portland cement is similar to that on a pure Al-system [4]. In the presence of calcite, monosulphate (Al-Ms and Fe-Ms) is expected to be unstable, and ettringite (Al-Ett) and monocarbonate (Fe-Mc and Al-Mc) form instead, which leads to a higher degree of space filling (Fig. 18). In contrast to a pure Al-system, however, Fe-ettringite is not expected to be stable in a mixed system, which results in Fe-Hc and Fe-Mc as the main Fe sinks in hydrated Portland cements. Note that at higher $CaSO_4$ contents ($SO_3/(Al,Fe)_2O_3 > 2$), Fe-ettringite can be stable in a Portland cement system. During the first hours of the hydration of Portland cements, an excess of $CaSO_4$ is present, which allows both Al- and Fe-ettringite to be formed. With progressing hydration, however, the $CaSO_4/(Al,Fe)_2O_3$ is reduced, which results in a situation where only Al-ettringite will be stable and both Al- and Fe-monocarbonate (or monosulphate in the absence of calcite) can be formed. The predicted presence of Fe-containing ettringite during the early hydration is consistent with the observations of Neubauer et al. [38]. The authors observed a peak shift of ettringite to a larger d-value during the first hours of OPC hydration, which could indicate the presence of Fe- (or of CO_3) in the ettringite structure. After a few hours, however, d-values decreased, thus suggesting the transformation to Al-ettringite.

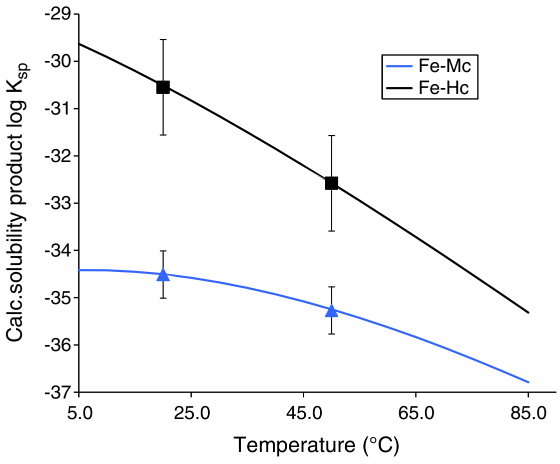

Fig. 16. Calculated solubility products of Fe-Mc and Fe-Hc from the solubility experiments. Squares: experimental solubility product of Fe-Hc, Triangles: experimental solubility product of Fe-Mc.

The presence of silicates was not included in the current assessment because data on the stability of Fe-containing Si-hydrogarnets (C_3FSH_4) and Fe-strätlingite (C_2FSH_8) were not yet available. There are indications, however, that the formation of Fe-containing Si-hydrogarnets is kinetically possible at ambient temperatures.

6. Conclusions

A crystalline Fe-Mc was synthesized by mixing appropriate amounts of C_2F, $CaCO_3$ and CaO at 20 °C, 50 °C and 80 °C. At ambient temperature the kinetics of the reaction was slow; C_2F transformation was completed only after one year and longer. After 3 months of equilibration, Fe-Hc was detected; after 1 year and longer Fe-Hc transformed to Fe-Mc. At 50 °C the kinetics were found to be faster. The presence of Fe-Hc and some Fe-Mc was already observed after 7 days. The amount of Fe-Mc increased while Fe-Hc disappeared over time. At 80 °C Fe-Mc was unstable with respect to Fe-hydroxide/hematite, portlandite and calcite.

The structure of Fe-Mc was solved and refined using synchrotron powder diffraction data. Fe-Mc was described in the rhombohedral $R\overline{3}c$ symmetry. It belongs to the AFm family with a positively charged main layer and a negatively charged interlayer. The structure of Fe-Mc was found to diverge from its Al analogous Al-Mc compound. The main difference consists in the carbonate location. Carbonate is bonded to the main layer in Al-Mc while it is weakly bonded in the interlayer in Fe-Mc.

EXAFS spectroscopy data supported the formation of stable Fe-Mc in which iron is octahedrally surrounded by six oxygen and calcium atoms. The Fe-Ca revealed that Fe is associated with the Fe-Mc structure while the absence of Fe–Fe backscattering contributions in

Table 10
Thermodynamic parameters of carbonate containing AFm phases at standard conditions (25 °C, 1 atm).

Phase	log K_{So}	$\Delta_fG°$ [kJ/mol]	$\Delta_fH°$ [kJ/mol]	S^0 [J/mol.K]	C^0_p [J/mol.K]	a_0[J/mol.K]	a_1[J/mol.K^2]	a_2 [J/mol.K]	a_3 [J/mol.K$^{0.5}$]	V^0 [cm^3/mol]	Ref.
C_4FcH_{12}	−34.59 ± 0.5	−6674.0	−7485	1230	950	612	1.160	−5.73e+05	0	292	[a]
$C_4Fc_{0.5}H_{10}$	−30.83 ± 0.5	−5952.9	−6581	1270	841	308	1.200	−9.08e+05	3200	273	[a]
C_4AcH_{11}	−31.47 ± 0.5	−7337.5	−8250	657	881	618	0.982	−2.59e+06	0	262	[b,c]
$C_4Ac_{0.5}H_{12}$	−29.13 ± 0.5	−7336.0	−8270	713	906	664	1.014	−1.30e+06	−800	285	[b,c]

[a] This study.
[b] Lothenbach et al. [6].
[c] Matschei et al. [9].

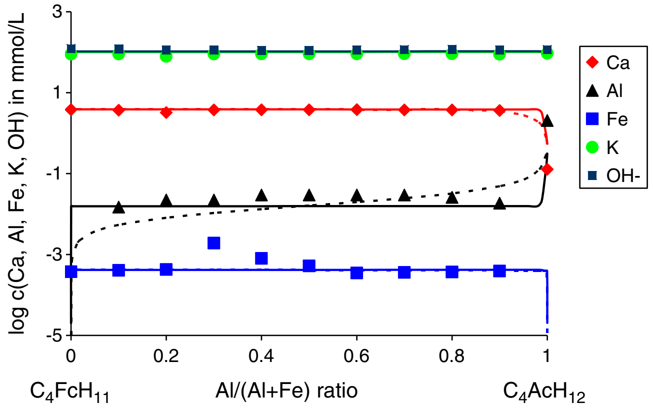

Fig. 17. Measured (points) and calculated (lines) concentrations in the liquid phases of the synthesized monocarbonate at different Al/Fe mole.

the synthesized material confirmed the absence of significant amounts of amorphous Fe-hydroxide [30]. The coordination environment of Fe in Fe-Mc corresponds to that of Al in the Al-analogue [30].

TGA and IR measurements revealed characteristics of the interlayer molecules of Fe-Mc and Al-Mc. The weight loss of the interlayer water molecules observed by TGA was found to occur in the temperature range around 240 °C for Fe-Mc and from 80 to 270 °C for Al-Mc. The IR spectra of Fe-Mc further showed vibrations of bonds are on same range of frequency with Al-Mc but different shape of peaks with the spectra of Al-Mc.

In the mixed $Ca_4[(Al_xFe_{1-x})_2(OH)_{12}]\cdot CO_3\cdot nH_2O$ system XRD data and measurements of the elemental composition in solution was not consistent with the formation of a solid solution formation between the Al- and Fe-Mc, presumably due to the structural differences between Al- and Fe-Mc. Al-Mc has triclinic structure and a layer thickness of 7.57 Å, while Fe-Mc has a rhombohedral structure and a layer thickness of 7.98 Å.

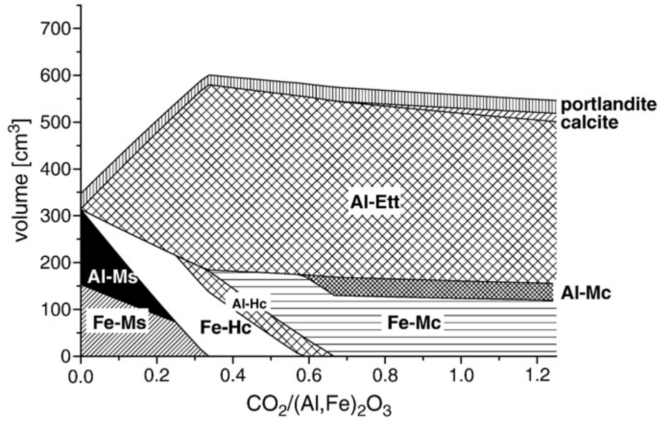

Fig. 18. Changes in the total volume of phases of a hydrated model mixture consisting of Al_2O_3, Fe_2O_3 and a fixed $SO_3/(Al,Fe)_2O_3$ ratio of 1 depending on the calcite content ($CO_2/(Al,Fe)_2O_3$ ratio). Constant amount of solids: $Al_2O_3 + Fe_2O_3 + CaSO_4 + CaO + CaCO_3$.

The solubility products were determined experimentally at 20 °C for Fe-Mc ($\log K_{S0,20°C} = -34.51$), for Fe-Hc (−30.55) and for Al-Mc (−31.55). At 50 °C, the $\log K_{S0,50\,°C}$ for Fe-Mc was −35.27 and for Fe-Hc −32.58. At standard conditions (25 °C, 1 atm) a $\log K_{S0}$ of −34.59 for Fe-Mc and of −30.83 for Fe-Hc was estimated. Thus, the experimentally derived solubility products of Fe-Mc and Fe-Hc were approximately 2-3 log units lower than those reported for Al-Mc and Al-Hc.

Thermodynamic modeling indicated that Al- and Fe-Mc are expected to dominate the composition of the phase assemblage in a system containing C_3A–C_2F–$CaCO_3$–$CaSO_4$–H_2O in the absence of $CaSO_4$. With the addition of $CaSO_4$, however, Al-Mc transformed to Al-ettringite.

Thermodynamic modeling further indicated that in a system containing C_3A–C_2F–$CaSO_4$–CaO–H_2O (absence of calcite), Al-Ms and Fe-Ms are expected to dominate the phase assemblage. In the presence of $CaCO_3$, however, Al-ettringite, Al-Mc and Fe-Mc are expected to be stable, while Fe-ettringite will not be present. Only at higher $SO_3/(Al,Fe)_2O_3$ ratios (>2), Fe-ettringite was predicted to be stable. High $SO_3/(Al,Fe)_2O_3$ ratios are achieved during the first hours of OPC hydration when only small amounts of the aluminate and ferrite clinkers have reacted. Hence, Fe-ettringite could potentially form in this stage of the hydration process. In the later stages, however, when a lower $SO_3/(Al,Fe)_2O_3$ ratio is achieved, Fe-Mc (or Fe-Ms in the absence of calcite) are expected to be stable, together with Al-ettringite and Al-Mc (or Al-Ms).

In summary, no experimental data have been available which could clearly indicate which Fe-containing phases might exist in hydrated cements. The data obtained in this study offer a possibility to predict the fate of iron oxides in Portland cement. Based on the available data, iron oxide can be expected to be present in hydrated cements rather as AFm phases than as ettringite. However, data for other important phases, such as Fe-siliceous hydrogarnet which might be more stable, are still missing. In the frame work of this study, the determination of thermodynamic data for other Fe-containing cement hydrates is ongoing and will help us in the future to predict the fate of iron oxide during the hydration. In addition to thermodynamic modelling, reliable experimental investigations of iron phases in hydrated cements are necessary. A study is carried out presently to identify Fe-bearing phases in hydrated cements using X-ray absorption spectroscopy (XAS).

Acknowledgements

The Swiss National Foundation is gratefully acknowledged for financial support. The authors would like to thank Luigi Brunetti, Dr. Mohsen Ben Haha for assistance with the laboratory work and Dr. Frank Winnefeld, Prof. Dr. Jürgen Neubauer, Dr. Friedlinde Götz-Neunhoeffer and Dr. Rainer Dähn for helpful discussions. The staffs of BM01 (SNBL) and BM26 (Dubble) at the ESRF are thanked for experimental assistance during the EXAFS and XRD measurements. The ESRF (Grenoble, France) is acknowledged for providing beam time at BM26.

References

[1] M. François, G. Renaudin, O. Evrard, A cementitious compound with composition $3CaO.Al_2O_3.CaCO_3.11H_2O$, Acta Crystallographica. Section C: Crystal Structure Communications 54 (9) (1998) 1214–1217.

[2] T. Matschei, B. Lothenbach, F.P. Glasser, Thermodynamic properties of Portland cement hydrates in the system $CaO–Al_2O_3–SiO_2–CaSO_4–CaCO_3–H_2O$, Cement and Concrete Research 37 (10) (2007) 1379–1410.

[3] B. Lothenbach, G. Le Saout, E. Gallucci, K. Scrivener, Influence of limestone on the hydration of Portland cements, Cement and Concrete Research 38 (6) (2008) 848–860.

[4] T. Matschei, B. Lothenbach, F.P. Glasser, The role of calcium carbonate in cement hydration, Cement and Concrete Research 37 (4) (2007) 551–558.

[5] H.J. Kuzel, H. Pöllmann, Hydration of C_3A in the presence of $Ca(OH)_2$, $CaSO_4 \cdot 2H_2O$ and $CaCO_3$, Cement and Concrete Research 21 (5) (1991) 885–895.

[6] B. Lothenbach, T. Matschei, G. Möschner, F.P. Glasser, Thermodynamic modelling of the effect of temperature on the hydration and porosity of Portland cement, Cement and Concrete Research 38 (1) (2008) 1–18.

[7] G. Möschner, B. Lothenbach, J. Rose, A. Ulrich, R. Figi, R. Kretzschmar, Solubility of Fe-ettringite ($Ca_6[Fe(OH)_6]_2(SO_4)_3 \cdot 26H_2O$), Geochimica et Cosmochimica Acta 72 (1) (2008) 1–18.

[8] F.P. Glasser, A. Kindness, S.A. Stronach, Stability and solubility relationships in AFm phases: Part I. Chloride, sulfate and hydroxide, Cement and Concrete Research 29 (6) (1999) 861–866.

[9] T. Matschei, B. Lothenbach, F.P. Glasser, The AFm phase in Portland cement, Cement and Concrete Research 37 (2) (2007) 118–130.

[10] H. Poellmann, Solid solution in the system $3CaO \cdot Al_2O_3 \cdot CaSO_4 \cdot aq–3CaO \cdot Al_2O_3 \cdot Ca(OH)_2 \cdot aq$, Neues Jahrbuch für Mineralogie Abhandlungen 161 (1989) 27–41.

[11] G. Möschner, B. Lothenbach, F. Winnefeld, A. Ulrich, R. Figi, R. Kretzschmar, Solid solution between Al-ettringite and Fe-ettringite ($Ca_6[Al_{1-x}Fe_x(OH)_6]_2(SO_4)_3 \cdot 26H_2O$), Cement and Concrete Research 39 (6) (2009) 482–489.

[12] A.P. Hammersley, S.O. Svensson, M. Hanfland, A.N. Fitch, D. Hausermann, Two-dimensional detector software: from real detector to idealised image or two-theta scan, High Pressure Research: An International Journal 14 (4) (1996) 235–248.

[13] M. Neville, IFEFFIT: interactive EXAFS analysis and FEFF fitting, Journal of Synchrotron Radiation 8 (2005) 322–324.

[14] B. Ravel, M. Neville, ATHENA, ARTEMIS, HEPHAESTUS: data analysis for X-ray absorption spectroscopy using IFEFFIT, Journal of Synchrotron Radiation 12 (4) (2005) 537–541.

[15] D.A. Kulik, GEMS-PSI 2.3, PSI Villigen, Switzerland, 2009, available at http://www.les.web.psi.ch/Software/GEMS-PSI/index.html.

[16] W. Hummel, U. Berner, E. Curti, F.J. Pearson, T. Thoenen, Nagra/PSI Chemical Thermodynamic Data Base 01/0, Universal Publishers/uPublish.com, Parkland, Florida, 2002.

[17] T. Thoenen, D.A. Kulik, Nagra/PSI Chemical Thermodynamic Data Base 01/01 for the GEM-Selektor (V.2-PSI) Geochemical Modeling Code: Release 28-02-03, Internal Report TM-44-03-04, 2003 available at http://www.les.web.psi.ch/software/GEMS-PSI/thermodata/index.html.

[18] D.A. Kulik, Thermodynamic properties of surface species at the mineral-water interface under hydrothermal conditions: a Gibbs energy minimization single-site 2pKA triple-layer model of rutile in NaCl electrolyte to 250 °C, Geochimica et Cosmochimica Acta 64 (18) (2000) 3161–3179.

[19] D.A. Kulik, Minimising uncertainty induced by temperature extrapolations of thermodynamic data: A pragmatic view on the integration of thermodynamic databases into geochemical computer codes, The use of thermodynamic databases in performance assessment, OECD, Paris, Barcelona, Spain, 2002.

[20] J. Ederova, V. Satava, Heat capacities of C_3AH_6, C_4ASH_{12} and $C_3AS_3H_{32}$, Thermochimica Acta 31 (1979) 126–128.

[21] H.C. Helgeson, J.M. Delany, H.W. Nesbitt, D.K. Bird, Summary and critique of the thermodynamic properties of rock forming minerals, American Journal of Science 278-A (1978) 229.

[22] M. Ecker, H.J. Pöllmann, Synthesis and characterisation of CO_3-containing Ca-Al-Fe-hydrates, International symposium of chemistry of cement, Göthborg, 1997, p. 2ii032.

[23] R. Fischer, H.J. Kuzel, Reinvestigation of the system $C_4A.nH_2O–C_4A.CO_2.nH_2O$, Cement and Concrete Research 12 (4) (1982) 517–526.

[24] M. Ecker, *Diadochiebeziehungen in Calciumaluminatferraten und deren Hydratationsprodukten.* PhD. thesis, Hallesches Jahrbuch für Geowissenschaften, Reihe B, Martin-Luther-Universität Halle-Wittenberg, 1998.

[25] D. Damidot, S. Stronach, A. Kindness, M. Atkins, F.P. Glasser, Thermodynamic investigation of the $CaO–Al_2O_3–CaCO_3–H_2O$ closed system at 25 °C and the influence of Na_2O, Cement and Concrete Research 24 (3) (1994) 563–572.

[26] H. Pöllmann, *Die Kristallchemie der Neubildungen bei Einwirkung von Schadstoffen auf hydrauliche Bindemittel.* PhD thesis, Erlangen-Nürnberg, 1984.

[27] J.P. Rapin, G. Renaudin, E. Elkaim, M. Francois, Structural transition of Friedel's salt $3CaO \cdot Al_2O_3 \cdot CaCl_2 \cdot 10H_2O$ studied by synchrotron powder diffraction, Cement and Concrete Research 32 (4) (2002) 513–519.

[28] G. Renaudin, F. Kubel, J.P. Rivera, M. Francois, Structural phase transition and high temperature phase structure of Friedel's salt, $3CaO \cdot Al_2O_3 \cdot CaCl_2 \cdot 10H_2O$, Cement and Concrete Research 29 (12) (1999) 1937–1942.

[29] G. Renaudin, M. Francois, O. Evrard, Order and disorder in the lamellar hydrated tetracalcium monocarboaluminate compound, Cement and Concrete Research 29 (1) (1999) 63–69.

[30] J. Rose, A. Bénard, S. El Mrabet, A. Masion, I. Moulin, V. Briois, L. Olivi, J.Y. Bottero, Evolution of iron speciation during hydration of C_4AF, Waste Management 26 (7) (2006) 720–724.

[31] A. Mesbah, C. Cau-dit-Coumes, F. Frizon, F. Leroux, J. Ravaux, G. Renaudin, A new investigation of the $Cl^-–CO_3^{2-}$ substitution in AFm phases. in press, doi:10.1111/j.1551-2916.2010.04305.x.

[32] A. Mesbah, J.-P. Rapin, M. François, C. Cau-dit-Coumes, F. Frizon, F. Leroux, G. Renaudin, Crystal structures and phase transition of cementitious bi-anionic AFm-(Cl^-,CO_3^{2-}) compounds, Journal American Ceramic Society 94 (1) (2011) 262–269.

[33] G. Renaudin, J.P. Rapin, B. Humbert, M. François, Thermal behaviour of the nitrated AFm phase $Ca_4Al_2(OH)12(NO_3)2–4H_2O$ and structure determination of the intermediate hydrate $Ca_4Al_2(OH)12(NO_3)2–2H_2O$, Cement and Concrete Research 30 (2) (2000) 307–314.

[34] G. Renaudin, R. Segni, D. Mentel, J.-M. Nedelec, L.F., C. T.-G., A Raman study of the sulfated cement hydrates: ettringite and monosulfoaluminate, Journal of Advanced Concrete Technology 5 (3) (2007) 299–312.

[35] H.F.W. Taylor, Crystal structures of some double hydroxide minerals, Mining Magazine 39 (304) (1973) 377–389.

[36] A.F. Hollemann, E. Wiberg, Lehrbuch der anorganischen Chemie, de Gruyter, Berlin, 1985.

[37] M.A. Trezza, A.E. Lavat, Analysis of the system $3CaO.Al_2O_3–CaSO_4.2H_2O–CaCO_3–H_2O$ by FT-IR spectroscopy, Cement and Concrete Research 31 (2001) 869–872.

[38] J. Neubauer, F. Götz-Neunhoeffer, D. Schmitt, M. Degenkolb, U. Holland, In-situ Untersuchung der frühen PZ-Hydratation, Internationale Baustofftagung (ibausil), Weimar, Germany, 2006, p. 16.